Iron-Loss Modeling With Sensorless Predictive Control of PMBLDC Motor Drive for Electric Vehicle Application

Prashant Kumar, *Graduate Student Member, IEEE*, Devara Vijaya Bhaskar, *Member, IEEE*, Utkal Ranjan Muduli, *Member, IEEE*, Abdul R. Beig, *Senior Member, IEEE*, and Ranjan Kumar Behera, *Senior Member, IEEE*

***Abstract*— Permanent-magnet brushless dc motor (PMBLDCM) is more suitable for electric vehicle (EV) with higher torque and driving performance. A suitable loss modeling of PMBLDCM with proper analysis can improve the control stability at different road surface conditions. However, the iron loss is not minimal enough to be ignored during high-speed operation of PMBLDCM drives. This article proposes a disturbance observer-based sensorless drive control for accurate estimation of the rotor position. This is achieved by taking the iron loss into consideration in order to further reduce the rotor position estimation error. A modified model predictive control is also proposed to deal with the novel modeling to provide torque ripple-free operation at reduced losses. The EV performances are compared for lossless and loss model of PMBLDCM through both simulation and experimental validation.**

***Index Terms*— Brushless dc motor drive, disturbance observer, iron-loss estimation, model predictive control, torque ripple minimization.**

I. Introduction

ELECTRIC transportation is gaining momentum as it will overcome problems due to conventional vehicles, such as global warming, resource shortages, and environmental pollution. The main tools for the development of electrification of transportation systems include exterior design, controller design, motor drives system, energy and power management processes, and system integration [1], [2]. The motor drive system is a key element for electric vehicle (EV) propulsion system since it is the predominant source of power in the EV [3]. Therefore, the study of high-performance motor drive for EV has been a subject of active research. Permanent-magnet (PM)-based propulsion motors, such as PM synchronous motor (PMSM), PM brushless dc motor (PMBLDCM) are used by EV manufacturers due to their high energy density. The drive configuration of PMSM is expensive and has less power density compared with that of PMBLDCM, especially in low-power vehicles. The low-cost drive arrangement makes the PMBLDCM propulsion system very attractive for use in cheaper EVs [4].

With trapezoidal back electromotive force (EMF) and quasi-square-wave current, PMBLDCM can produce a constant electromagnetic torque. The high-frequency torque ripple in PMBLDCM is induced due to manufacturing procedures, control strategies, and problems due to the commutation of switches [5], [6]. The torque ripple generates noise, mechanical vibration, and speed fluctuations that need to be addressed. Accurate modeling of PMBLDCM considering design aspects and material properties is much more relevant to address these issues in order to enhance the performance of PMBLDCM drives for EV applications. Researchers have shown that a detailed model considering the iron loss, which consists of hysteresis and eddy-current losses, plays a significant role in the performance of PMBLDCM [5], [7]–[12]. The modeling presented in [7] significantly considers lower order harmonics, which can cause additional eddy-current losses to PM and conductive rotor sleeves when the PMBLDCM operates at a high-speed and heavy-duty region. In [8] and [9], the optimal iron-loss model is estimated based on a finite-element analysis, considering nonsinusoidal back EMFs and current. The major challenge of this approach is that a considerable amount of time must be dedicated to the finite-element-based simulation under different operating conditions. Temperature dependence iron-loss modeling is addressed in [10] and [11]. In [10], only the temperature dependence of the eddy-current loss is considered, while the hysteresis loss is presumed not to be affected by the temperature. In [11], the effect of temperature on total iron loss is modeled by the implementation of an analogous temperature-dependent coefficient, a combination of temperature effects on both hysteresis and eddy-current losses. A nonlinear phase variable model is proposed in [12] to analyze the effect of stator and rotor losses on PMBLDCM.

Manuscript received July 13, 2020; revised September 24, 2020; accepted October 30, 2020. Date of publication November 9, 2020; date of current version August 24, 2021. This work was supported by the Abu Dhabi Education and Knowledge (ADEK), United Arab Emirates, under Grant AARE18-102. *(Corresponding author: Prashant Kumar.)*

Prashant Kumar is with the Department of Electrical Engineering, IIT (ISM) Dhanbad, Dhanbad 826004, India, and also with the Department of Electrical Engineering and Computer Science, Khalifa University, Abu Dhabi, United Arab Emirates (e-mail: ku.prashantr@gmail.com).

Devara Vijaya Bhaskar is with the Department of Electrical Engineering, IIT (ISM) Dhanbad, Dhanbad 826004, India.

Utkal Ranjan Muduli and Ranjan Kumar Behera are with the Department of Electrical Engineering, IIT Patna, Patna 801103, India (e-mail: utkal.pee17@iitp.ac.in).

Abdul R. Beig is with the Advanced Power and Energy Center, Department of Electrical Engineering and Computer Science, Khalifa University, Abu Dhabi, United Arab Emirates (e-mail: balanthi.beig@ku.ac.ae).

Digital Object Identifier 10.1109/TTE.2020.3036991

Depending on the flux variance, the stator phase currents and the speed of the motor, the iron-loss model is developed precisely in order to model fractional-slot machines. The effect of the temperature on the iron loss and the limitation of the existing model on the estimation of the iron loss without considering the temperature effect are demonstrated in [5]. Considering all aspects of modeling, simplified modeling reflecting the impact of iron loss is proposed in this article, which provides a reliable estimate of the magnitude and corresponding angle contribution due to iron loss.

The use of position sensors for the electric traction system has been verified for years in the case of EVs. However, in order to build a smart and autonomous onboard fault detection and diagnostic system, the EVs need to be more reliable in the context of a fail-safe operation. Such performance can be achieved by sensorless operation. Researchers around the globe therefore sought to provide an effective, sensor-free framework for PMBLDCM-fed EV applications [13]–[18]. The research approaches concentrate primarily on either the enhancement of the motor architecture or active ripple compensation of the torque. Back EMF sensing-based hybrid sliding mode control for PMBLDCM in vehicle applications is proposed in [13], which is more sensitive to parameter uncertainties at lower speed. The sensorless antilock braking control system based on back EMF given in [14] for estimating the rotor speed of PMBLDCM is validated for low-speed application and uses wavelet transformation, which does not require the deployment of separate break sensors in every section of the vehicle. In [15], a sensorless scheme is designed to compensate for commutation error along with zero-crossing detection from line-to-line back EMF. In addition, Song *et al.* [17] implemented a commutation error compensation technique based on the harmonic analysis of phase back EMF. However, lower amplitude harmonic content prevents its use for high-speed applications as it is less susceptible to phase delay due to low-pass filtering. Jafarboland and Silabi [16] implemented a sensorless operation to minimize commutation torque ripple using line-to-line flux linkage. The aim of this approach is to obtain a precise rotor orientation and to determine the motor parameters by using the Kalman filter for line-to-line flux linkage. The extended Kalman filter involves a complex computation thus not appropriate for real-time implementation as the interrupt routine time for a wide-speed range motor is very limited.

Recently, a stable state-feedback controller to mitigate the effects of disturbances is designed for PMSM using sensorless disturbance observer [18]. These techniques have not yet fundamentally solved the issue of the iron loss of the motor, so there is scope for further study as the effect of motor iron loss has been ignored. A disturbance observer-oriented sensorless approach is proposed in this article and experimentally validated for a wide range of PMBLDCM speed variations. The proposed disturbance observer estimates the rotor position along with the rotor speed by considering the iron-loss effect. The torque ripple minimization of PMBLDCM-based EVs has received considerable attention from researchers to ensure a smooth and convenient ride for passengers [19]. Various closed-loop control techniques, such as vector control [20], [21], direct torque control [22], and Fourier series-based control [23], are available in the literature to reduce the torque ripple of PMBLDCM. A unique petal-wave current-dependent vector control approach is presented in [20] without considering the effect of iron-loss component. However, Buja *et al.* [20] provided a descriptive study of copper loss minimization when achieving a maximum torque per ampere. Even achieving a lower copper loss, the proportional-integral (PI)-dependent vector control approach has a disadvantage of higher settling time, leading to higher torque ripples at reduced bandwidth. In order to address these issues, a finite control set model predictive control (FCS-MPC) technique has recently been introduced [24]–[30]. FCS-MPC is easy to configure, provide fast transient response, and optimal motor current control to maintain a large bandwidth. The FCS-MPC for induction machine (IM) is explored in [24]. This process has been implemented with space vector pulsewidth modulation and utilizes the Kalman filter to obtain state responses that estimate the nonmeasured load torque. FCS-MPC developed in [25] is proposed for PMSM drives using constant input and online optimization control regulations. The technique improves the reliability of prediction-oriented scheme with an independent modulation state, given the uncertainty of the optimization problem. The performance of FCS-MPC for PMBLDCM relies on the estimation of the optimum voltage vector (VV), which significantly minimizes the cost function [27]. The predictive deadbeat control method for PMBLDCM is proposed in [28], with an accurate estimate of the switching frequency from the selected VV over the next sampling interval. FCS-MPC presented in [29] integrates a ranking analysis to reduce the uncertainty due to the tuning of weighting factors. However, this approach does not recognize the effect of iron loss, nor does it include any information on temperature dependence when used for EV applications.

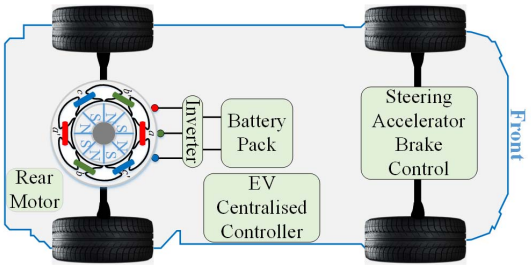

Fig. 1. Schematic for PMBLDCM-driven EV topology.

A modified MPC controller for PMBLDC motor drive considering standard automotive temperature range is proposed in this article. The improved dynamic model of the PMBLDCM by taking iron loss into consideration is used. The PMBLDCM model, effect of iron loss on the torque and stator current, is given in Section II. An improved optimum current vector-based FCS-MPC by considering the effect of iron loss is proposed in Section III. A three-phase three-level (TPTL) neutral-point-clamped (NPC) voltage-source inverter (VSI) is used to drive the PMBLDCM. The TPTL-VSI gives greater flexibility in the determination of switching vectors, lower voltage stress, and improved total harmonic distortion

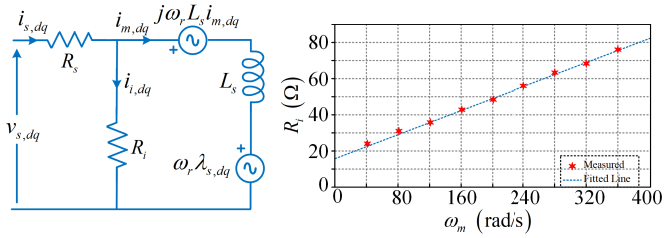

Fig. 2. (a) Internal circuit model of PMBLDCM in the dq frame. (b) R_i at different values of ω_m.

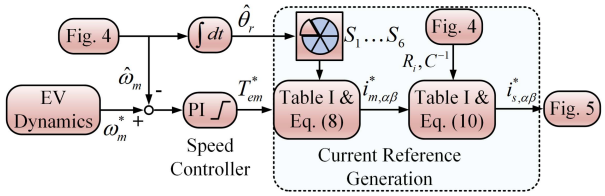

Fig. 3. Speed controller and current reference generation.

(THD) compared with that of two-level VSI [31]. The low THD helps in reducing the torque ripple. The proposed MPC controller not only achieves reduced torque ripple and minimal copper losses but also includes a technique to minimize the operating switching frequency of the drive. In addition, dc-link capacitor voltage balancing by considering additional objectives in its main objective function is also achieved. This decrease in the switching frequency reduces the switching loss, thus reducing the total drive temperature. A disturbance observer-based sensorless approach is proposed for precise rotor position estimation, which is detailed in Section III. The proposed sensorless MPC scheme is verified both by simulation and hardware experiments. The results are given in Section IV. Finally, the conclusions are given in Section V.

II. PMBLDCM Modeling Considering Iron-Loss Effects

A schematic of PMBLDCM driven rear motor-driven EV is shown in Fig. 1. It comprises a PMBLDCM, an TPTL VSI stack, and a battery pack as dc power source. The equivalent circuit model of the PMBLDCM in the dq plane is shown in Fig. 2(a) by considering the iron losses.

A. Calculation of R_i and Iron-Loss Modeling of PMBLDCM

The equivalent resistance representing iron loss (R_i) for a given PMBLDCM is determined experimentally as follows. At steady state and no-load condition, when the motor is running at constant speed of ω_m, the iron loss ($P_i = P_{\text{in}} - 3R_s I_{s,\text{rms}}^2$) is computed from Fig. 2(a). The input power (P_{in}) along with root mean square (rms) value of stator phase voltages and currents ($V_{s,\text{rms}}$ and $I_{s,\text{rms}}$) can be measured using a power analyzer. From Fig. 2(a), the iron loss at steady state can be written as in the following equation:

$$P_i = \frac{(e_{s,dq})^2}{R_i} = \left(\frac{1}{R_i}\right)\omega_r^2[(\lambda_{s,d})^2 + (\lambda_{s,q})^2] = \left(\frac{1}{R_i}\right)\left[V_{s,\text{rms}}^2 - 2R_s P_{\text{in}} + 3R_s^2 I_{s,\text{rms}}^2\right] \quad (1)$$

where R_s is the stator phase resistance, L_s is the stator inductance, $e_{s,dq}$ is the back EMF, and ω_r is the electrical speed of the rotor. The back emf is given by $e_{s,dq} = (\omega_r \lambda_{s,dq})$, where $\lambda_{s,dq}$ $(= \lambda_{s,d} + j\lambda_{s,q})$ represents the back EMF per ω_r. It can be noted from the established relation in (1) that R_i can be evaluated from the slope of the P_i versus $(e_{s,dq})^2$ curve, i.e., P_i versus ω_r^2 curve. R_i is calculated at various motor speeds ω_m varying from 40 to 360 rad/s. These R_i values are plotted against ω_m in Fig. 2(b), and a linear regression polynomial is obtained as in (2) using curve-fitting algorithms. The curve extrapolated until $\omega_m = 0$ rad/s, and thus, an offset resistance of 17.12 Ω is reported. R_i is estimated from ω_m as in the following equation [32]:

$$R_i = 0.145\omega_m + 17.12. \quad (2)$$

In steady state, the magnetizing component of the stator current ($i_{m,dq}$) is obtained from Fig. 2(a) as in (3). The relation in (4) introduces a variable C that represents the variable due to iron loss with magnitude $k_c = (1 + (\omega_r L_s/R_i)^2)^{1/2}$ and angle advancement of $\theta_c = \tan^{-1}(\omega_r L_s/R_i)$

$$i_{m,dq} = C\left(i_{s,dq} - \omega_r R_i^{-1}\lambda_{s,dq}\right) \quad (3)$$

$$C = \begin{cases} k_c^{-1}e^{-j\theta_c}, & \text{iron-loss model} \\ 1, & \text{model ignoring iron loss.} \end{cases} \quad (4)$$

From Fig. 2(a) and relation (3), the dynamics of PMBLDCM can be represented as in (5) where the stator current ($i_{s,dq} = i_{s,d} + ji_{s,q}$) is the state of the equation and $v_{s,dq}$ is the controlled stator voltage. τ_s $(= L_s/R_s)$ represents the electrical time constant of PMBLDCM

$$\frac{di_{s,dq}}{dt} = -\left(C^{-1}\tau_s^{-1} + j\omega_r\right)i_{s,dq} + L_s^{-1}(C^{-1}v_{s,dq} - e_{s,dq}). \quad (5)$$

The electromagnetic torque (T_{em}) developed can be deduced by considering the iron loss as in the following equation:

$$T_{\text{em}} = \Re(\bar{\lambda}_{s,dq} i_{m,dq}) = \Re(C\bar{\lambda}_{s,dq} i_{s,dq}) - T_i. \quad (6)$$

The notation $\Re$ denotes the real part of the complex variable and $\bar{\lambda}_{s,dq}$ represents the complex conjugate of $\lambda_{s,dq}$. The additional electromagnetic torque component due to iron loss (T_i) varies with sectors ($k = S_1, \ldots, S_6$) as in the following equation:

$$T_i|_{S_1,\ldots,S_6} = \omega_r R_i^{-1}|\lambda_{s,dq}|^2_{S_1,\ldots,S_6}. \quad (7)$$

It should be noted that, when iron-loss effect is ignored, in (3), $i_{m,dq} = i_{s,dq}$. Therefore, the first term in right-hand side of (6), and $\Re(\bar{\lambda}_{s,dq} i_{s,dq})$ represents the electromagnetic torque produced by motor when the iron-loss effect is ignored, denoted by T_{es} $(=\Re(\bar{\lambda}_{s,dq} i_{s,dq}) = \lambda_{s,d} i_{s,d} + \lambda_{s,q} i_{s,q})$.

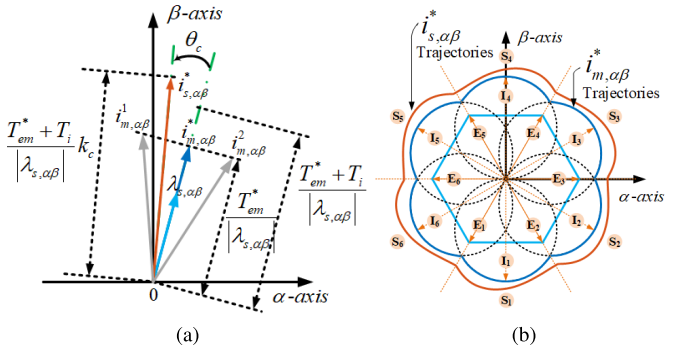

Fig. 4. (a) Optimal reference current considering iron loss. (b) Trajectory of the back EMF and current vector for six sectors.

TABLE I

$\lambda_{s,\alpha\beta}$ AND $i^*_{s,\alpha\beta}$ IN SIX DIFFERENT SECTORS

Sector	$\hat{\theta}_r$	$\lambda_{s,\alpha}/\lambda_n$	$\lambda_{s,\beta}/\lambda_n$	$i^*_{m,\alpha}/I^*$	$i^*_{m,\beta}/I^*$
S_1	$-\frac{2\pi}{3} \rightarrow -\frac{\pi}{3}$	2μ	$-2/\sqrt{3}$	$\frac{2\mu}{3\mu^2+1}$	$\frac{-2/\sqrt{3}}{3\mu^2+1}$
S_2	$-\frac{\pi}{3} \rightarrow 0$	$(\mu+\frac{1}{3})$	$\sqrt{3}(\mu-1)$	$\frac{3\mu+1}{9\mu^2-12\mu+7}$	$\frac{\sqrt{3}(3\mu-3)}{9\mu^2-12\mu+7}$
S_3	$0 \rightarrow \frac{\pi}{3}$	$-(\mu-\frac{7}{3})$	$\sqrt{3}(\mu-1)$	$\frac{-(3\mu-7)}{9\mu^2-24\mu+19}$	$\frac{\sqrt{3}(3\mu-3)}{9\mu^2-24\mu+19}$
S_4	$\frac{\pi}{3} \rightarrow \frac{2\pi}{3}$	$-2(\mu-2)$	$2/\sqrt{3}$	$\frac{-(2\mu-4)}{3\mu^2-12\mu+13}$	$\frac{2\mu/\sqrt{3}}{3\mu^2-12\mu+13}$
S_5	$\frac{2\pi}{3} \rightarrow \pi$	$-(\mu-\frac{5}{3})$	$-\sqrt{3}(\mu-3)$	$\frac{-(3\mu-5)}{9\mu^2-48\mu+67}$	$\frac{-\sqrt{3}(3\mu-9)}{9\mu^2-48\mu+67}$
S_6	$\pi \rightarrow -\frac{2\pi}{3}$	$(\mu-\frac{13}{3})$	$-\sqrt{3}(\mu-3)$	$\frac{3\mu-13}{9\mu^2-60\mu+103}$	$\frac{-\sqrt{3}(3\mu-9)}{9\mu^2-60\mu+103}$

B. Optimal Current Vector Formulation

A cascaded control structure as shown in Fig. 3 is used for the speed control of PMBLDC. The estimated speed feedback ($\hat{\omega}_m$) is compared with the speed reference (ω^*_m). The optimal dynamic speed response is achieved by using a PI controller. The output of the speed controller is the torque reference T^*_{em}, which does not account for the copper loss and iron loss [20]. Therefore, an acceptable modification must be introduced, as described in the following. The optimal reference current magnitude I^* can be calculated from T^*_{em} by using the following equation:

$$T^*_{\text{em}} = P^*_e \omega_m^{-1} = 2\lambda_n I^* \tag{8}$$

where P^*_e $(=2EI^*)$ is the electrical power of PMBLDCM ignoring the losses, E $(=\lambda_n \omega_m)$ is the back EMF magnitude, and λ_n is the nominal value of back EMF constant. Certainly, further analysis is made in the $\alpha\beta$ plane to obtain a proper visual representation and the previous derived equations can be used without any modification. The variables in the $\alpha\beta$ plane can be obtained by multiplying $e^{j\hat{\theta}_r}$ to the variables in the dq plane. The discussion on the estimated rotor electrical position of PMBLDCM ($\hat{\theta}_r$) is presented in Section III-A. Considering T^*_{em} as the command signal, there is possibility of infinite current vector ($i^1_{m,\alpha\beta}$, $i^2_{m,\alpha\beta}$, …, $i^*_{m,\alpha\beta}$, …, $i^\infty_{m,\alpha\beta}$) as shown in Fig. 4(a) with a projection length of $T^*_{\text{em}}/\left|\lambda_{s,\alpha\beta}\right|$. However, only one optimal current vector ($i^*_{m,\alpha\beta}$) is available, which is in phase with $\lambda_{s,\alpha\beta}$. The $i^*_{m,\alpha\beta}$ vector provides the minimum copper loss with constant torque and can be derived from (8) and Table I, as given in (9). The $\alpha\beta$ components of $\lambda_{s,\alpha\beta}$ and the $i^*_{m,\alpha\beta}$ in six different sectors over one cycle of the supply current is defined in Table I, where the variable $\mu = 2\hat{\theta}_r/\pi$. The trajectory in each sector in (10) represents a circle with centroid $(0, I^*/\sqrt{3})$, shown in Fig. 4(b)

$$i^*_{m,\alpha\beta}\big|_{k=S1} = \frac{T^*_{\text{em}}}{|\lambda_{s,\alpha\beta}|} u_\lambda = \frac{T^*_{\text{em}}}{|\lambda_{s,\alpha\beta}|^2} \lambda_{s,\alpha\beta} \tag{9}$$

$$\left(i^*_{m,\alpha}\right)^2_{S1} + \left(i^*_{m,\beta} + \frac{I^*}{\sqrt{3}}\right)^2_{S1} = \left(\frac{I^*}{\sqrt{3}}\right)^2 \tag{10}$$

where u_λ is the unit vector in the direction of $\lambda_{s,\alpha\beta}$. The obtained $i^*_{m,\alpha\beta}$ is evaluated by avoiding the iron loss that results in: 1) inaccuracies in rotor position estimation; 2) reduces the generation of torque than the actual as per (6); and 3) ripple due to error in estimated rotor position. A solution must therefore be introduced to overcome this issue by incorporating additional torque due to iron loss, i.e., T_i as in (7). Again, as shown in Fig. 4(a), there will be infinite current vectors with a projection length of $C^{-1}(T^*_{\text{em}} + T_i)/|\lambda_{s,\alpha\beta}|$. However, only one optimal current vector $i^*_{s,\alpha\beta}$, which is in phase advance of θ_c with $\lambda_{s,\alpha\beta}$, can provide minimal copper loss considering the iron-loss effect. $i^*_{s,\alpha\beta}$ also substantially decreases the torque ripple and can be calculated from (6) as per the following equation:

$$i^*_{s,\alpha\beta} = C^{-1} i^*_{m,\alpha\beta} + R_i^{-1} e_{s,\alpha\beta}. \tag{11}$$

III. SENSORLESS PREDICTIVE CONTROL OF PMBLDCM INCLUDING IRON LOSS

A sensorless architecture is conducted using a disturbance observer to estimate unknown disturbances due to loss in functioning units [18]. The operational schematic for the proposed disturbance observer-based sensorless operation of PMBLDCM is presented in Fig. 5. In addition, the control structure of the proposed MPC is shown in Fig. 7. The overall control system utilizes the speed controller, current controller, rotor speed estimation, rotor flux estimation, prediction model, TPTL switching logic table, and the cost function minimization blocks. The proposed disturbance observer is utilized to estimate the rotor position ($\hat{\theta}_r$) and rotor speed ($\hat{\omega}_r$).

A. Estimation of Rotor Position, Motor Speed, and Iron-Loss Resistance

Flux position is detected to extract the exact position of the rotor since no hall sensors are used. $\hat{\theta}_r$ and $\hat{\omega}_r$ estimation is performed in the dq plane to avoid complexities of the disturbance observer. The expression given in (5) can be rearranged as (12) where the disturbances ($\hat{\delta}_{s,dq} = \hat{\delta}_{s,d} + j\hat{\delta}_{s,q}$) is separated from the original modeling without considering the iron losses

$$\frac{di_{s,dq}}{dt} = \underbrace{-\left(\tau_s^{-1} + j\omega_r\right) i_{s,dq} + L_s^{-1}\left(v_{s,dq} - e_{s,dq}\right)}_{\text{lossless model}} + \underbrace{\left(C^{-1} - 1\right)\left(-\tau_s^{-1} i_{s,dq} + L_s^{-1} v_{s,dq}\right)}_{\text{disturbance } \hat{\delta}_{s,dq} \text{ due to iron loss}} \tag{12}$$

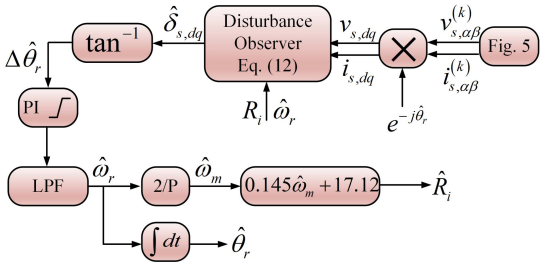

Fig. 5. Estimation of ω_m and R_i using disturbance observer.

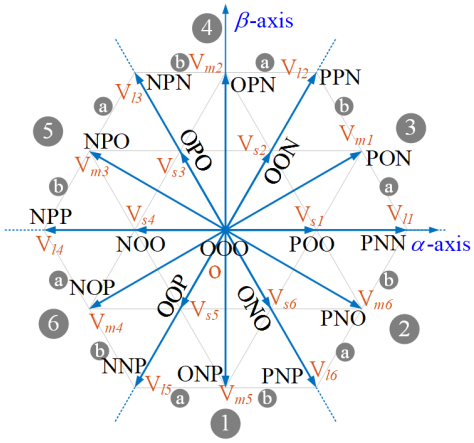

Fig. 6. Switching states of TPTL VSI.

Substituting C in (12), $\hat{\delta}_{s,dq}$ can be related to the speed of the motor ($\hat{\omega}_r$) and R_i as in the following equation:

$$\begin{aligned}\hat{\delta}_{s,dq} &= j\hat{\omega}_r R_i^{-1}(-R_s i_{s,dq} + v_{s,dq}) \\ \Delta\hat{\theta}_r &= \tan^{-1}(\hat{\delta}_{s,q}/\hat{\delta}_{s,d}).\end{aligned} \tag{13}$$

Variations in rotor position ($\Delta\hat{\theta}_r$) can be computed with the obtained $\hat{\delta}_{s,dq}$ that can therefore be used to measure ω_r. In Fig. 5, $\hat{\omega}_r$ is estimated from the relative disturbance error using an PI controller followed by a low-pass filter $(\omega_r/(s+\omega_r))$. $\hat{\omega}_r T_s$ is added with estimated rotor position $\hat{\theta}_r$ to compensate for the delay due to different pulsewidth modulation techniques. The actual estimated motor speed ($\hat{\omega}_m$) is described by $\hat{\omega}_m = \hat{\omega}_r/p$, where p represents the number of pole pairs.

B. Model Predictive Control With Iron-Loss Consideration

In traditional MPC, the cost function associated with the current control does not provide accurate control of PMBLDCM without considering the iron loss. A modified MPC is therefore proposed in this article to resolve the effect of iron loss in current controls, as shown in Fig. 7. For this process, the switching frequency control is also achieved along with the dc-link capacitor voltage balancing of the NPC TPTL-VSI-based EV drive. The TPTL-VSI uses three different states ('P' {1100}, 'O' {0110}, and 'N' {0011}) to represent the four insulated-gate bipolar transistor (IGBT) switches of each leg. The binary number "1" shows that the switch is "ON," whereas the binary number "0" shows switch

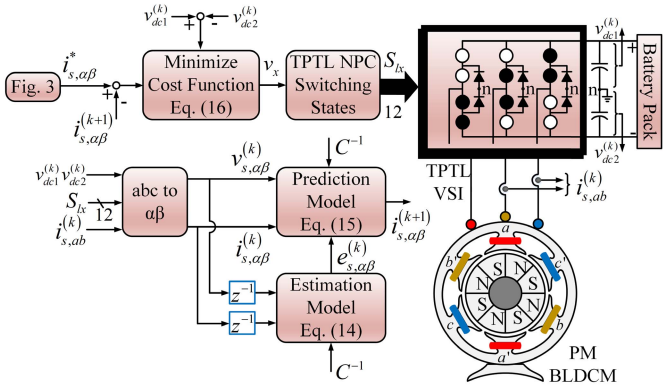

Fig. 7. MPC structure of PMBLDCM drive with considering iron loss.

status as "OFF." The TPTL-VSI has 27 VVs corresponding to available switching states. In order to reduce/nullify common-mode voltage (CMV), only 19 VVs are used for the proposed MPC, as shown in Fig. 6. These VVs are grouped as: 1) large vectors V_{lk}; 2) medium vectors V_{mk}; 3) small vectors V_{sk}; and 4) zero vector (O). The entire $\alpha\beta$-plane is converted into six different sectors ($k = 1 \ldots 6$) at $\pi/3$ intervals, and every sector is subdivided into two subsectors (a, b) at $\pi/6$ intervals. From the estimated rotor position information, the sector and subsector is identified and the voltage space vector $v_{s,\alpha\beta}^{(k)}$ is evaluated by using the proper selection of the vector index V_x, where $x \in \{l1 \ldots l6, m1 \ldots m6, s1 \ldots s6, O\}$ is the VVs index, as shown in Figs. 6 and 7. The MPC structure, given in Fig. 7, mainly consists of stator back EMF ($\hat{e}_{s,\alpha\beta}$) estimation, supply current vector ($i_{s,\alpha\beta}$) prediction, and cost function minimization. Let us define $di_{s,\alpha\beta}/dt = (i_{s,\alpha\beta}^{(k+1)} - i_{s,\alpha\beta}^{(k)})/T_s$ and the back EMF can be estimated as in the following equation:

$$\hat{e}_{s,\alpha\beta}^{(k-1)} = \frac{L_s}{T_s}\left(1 - \frac{C^{-1}T_s}{\tau_s}\right) i_{s,\alpha\beta}^{(k-1)} - \frac{L_s}{T_s} i_{s,\alpha\beta}^{(k)} + C^{-1} v_{s,\alpha\beta}^{(k-1)}. \tag{14}$$

As back EMF varying slowly with higher time constant compared to sampling instant T_s, one step delay/advance will not affect the overall performances of the controller, i.e., $\hat{e}_{s,\alpha\beta}^{(k)} \approx \hat{e}_{s,\alpha\beta}^{(k-1)}$. For one step prediction of stator current, let us define $di_{s,\alpha\beta}/dt = i_{s,\alpha\beta}^{(k+1)} - i_{s,\alpha\beta}^{(k)}/T_s$ and the current feedback signal can be estimated as follows:

$$i_{s,\alpha\beta}^{(k+1)} = \left(1 - \frac{C^{-1}T_s}{\tau_s}\right) i_{s,\alpha\beta}^{(k)} + \frac{T_s}{L_s}\left(C^{-1} v_{s,\alpha\beta}^{(k)} - \hat{e}_{s,\alpha\beta}^{(k)}\right). \tag{15}$$

The objective function of the proposed MPC considering iron-loss component is expressed with three objective, i.e., current control, switching frequency control, and dc-link voltage balancing control. The proposed method considers sampling frequency in such a way that the switching frequency (f_{sw}) of generated pulse is within the maximum limit as per the Nyquist criteria. By considering sampling time of $T_s = 50\ \mu$s, maximum f_{sw} must be less than 10 kHz. Further reduction in f_{sw} of overall drive performance can be achieved by introducing additional objective to the main objective function.

TABLE II
PARAMETERS FOR SIMULATION AND EXPERIMENT

PM BLDC Motor, 8 pole, 2.5kW, 1500 rpm,
$\lambda_n = 0.175 V.s/rad$, $J = 0.089 Kg.m^2$.
$B = 10^{-3} Nm.s/rad$, $R_s = 2.4\Omega$, $L_s = 8.5$ mH.

The cost minimization function expressed in (16) is to enable the torque ripple-free operation of PMBLDCM drives with reduced copper losses

$$\min g = \underbrace{W_i\left(i^*_{s,\alpha\beta} - i^{(k+1)}_{s,\alpha\beta}\right)^2}_{\text{Current Control}} + \underbrace{W_f\left(V_s^{(k-1)} - V_s^{(k)}\right)}_{\text{Switching Frequency Control}} + \underbrace{W_v\left(v^{(k)}_{\text{dc1}} - v^{(k)}_{\text{dc2}}\right)}_{\text{DC-link Voltage Balancing}} = W_i g_i + W_f g_f + W_v g_v \quad (16)$$

where $V_s^{(k)}$ is the stator voltage of PMBLDCM at the kth switching instant. The dc-link voltages v_{dc1} and v_{dc2} are measured through two voltage sensors and can be feedback to the MPC controller directly through appropriate dc filter. The weighting factors (W_i, , W_f, W_v) corresponding to the current control and switching frequency control are set to 0.33 to eliminate the shortcomings of online/offline tuning. This approximation can be validated by applying two-stage prediction method with ranking analysis, as mentioned in [29].

1) The first step of the proposed method is the selection of the VVs groups from (16). The speed and torque robustness of the PMBLDCM drive can be greatly affected by VV selection. Large vectors can be selected for high torque changeover at higher speed if $g \geq 0.7$. The medium vectors can be selected with $0.3 \leq g < 0.7$, if dc-link capacitor voltage balancing is necessary. The small vectors are specifically important at low-speed requirement of EV drive and it can be selected on $0 \leq g < 0.3$.
2) The second step of the proposed method is to apply the similar ranking analysis as in [29], where three ranks (R_1, R_2, R_3) are assigned to the objectives g_i, g_f, g_v. The average value of these ranks, i.e., $R = (R_1 + R_2 + R_3)/3$ is evaluated for each of the VVs in the selected voltage groups. Finally, the optimum selection of VV can be obtained by minimizing the average rank "R."

IV. RESULTS AND DISCUSSION

The validation of the proposed MPC controller in addition to the disturbance observer is verified by simulation and experimental findings. All the internal parameters of the PMBLDCM are extracted through various open-loop tests. The parameters obtained are shown in Table II. These PMBLDCM parameters are used in the simulation. The proposed MPC-based closed-loop drive performance is verified through simulation in the MATLAB/Simulink environment.

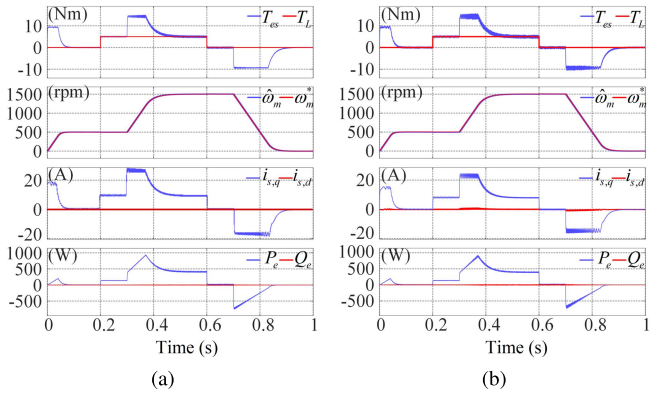

Fig. 8. Simulation results of T_{es}, T_L, $\hat{\omega}_m$, $\omega_m{}^*$, $i_{s,dq}$, P_e, and Q_e of PMBLDCM with sensorless MPC. (a) With considering iron loss. (b) Without considering iron loss.

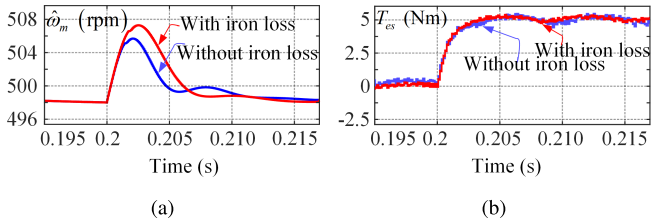

Fig. 9. Comparison of (a) speed and (b) torque at load change from 0 to 5 Nm with or without considering iron loss.

A. Simulation Results

The PMBLDCM drive is simulated to evaluate the proposed MPC considering iron losses and the corresponding results are compared with lossless model presented in [20]. Fig. 8(a) reflects the simulation performance while considering iron loss by considering the proposed MPC controller. Fig. 8(b) shows a simulation validation without taking the iron losses into account with PI controller-based vector control approach. The efficiency of the proposed MPC is assessed with load changes at different speed ranges to determine the robustness of PMBLDCM, by considering iron loss or without iron loss. At $t = 0.07$ s, the no load PMBLDCM drive speed is at steady state with $\hat{\omega}_m = 500$ rpm. A sudden load change with a load torque of $T_L = 5$ Nm is applied at $t = 0.2$ s. It is observed that the proposed disturbance observer-based speed estimation provides accurate tracking in speed during sudden load change, as shown in Fig. 9. A step change in motor speed from 500 to 1500 r/min is commanded with the same load of $T_L = 5$ Nm at $t = 0.3$ s, and the motor achieves its stable operating speed in the duration of 0.17 s. In order to observe the robustness of the proposed observer, PMBLDCM is suddenly unloaded at $t = 0.6$ s. The proposed disturbance observer has good dynamic behavior as $\hat{\omega}_m$ tracks ω^*_m with almost zero steady-state error and meets the desired transient response. At $t = 0.7$ s, a negative step change in ω^*_m from 1500 r/min to zero speed is commanded with $T_L = 0$ Nm, i.e., at no load. The simulation results of motor torque (T_{em}), active power (P_e), reactive power (Q_e), and dq-axis stator currents ($i_{s,d}$ and $i_{s,q}$) are also given in Fig. 8. The comparative

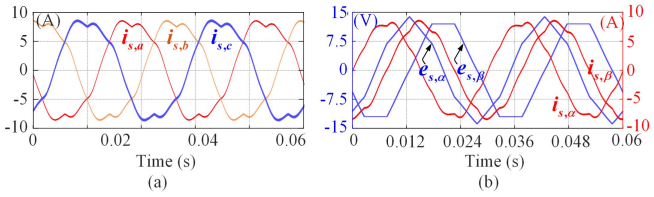

Fig. 10. Simulation results. (a) Expanded view of stator currents in the abc-frame. (b) $\alpha\beta$-components of stator currents and phase back EMF for sensorless MPC under steady state at $T_L = 5$ Nm.

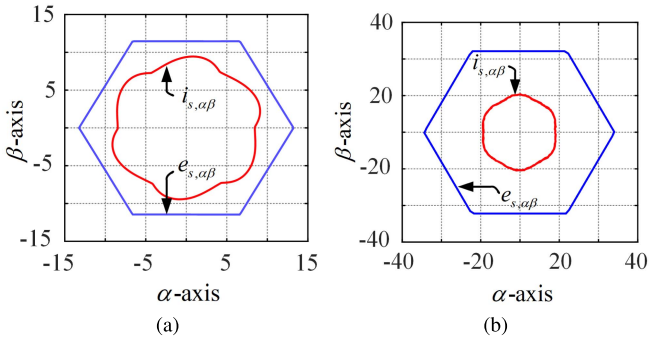

Fig. 11. Simulation results. The trajectory plot for phase back EMF and stator phase currents at (a) $\hat{\omega}_m = 500$ r/min and (b) $\hat{\omega}_m = 1500$ r/min.

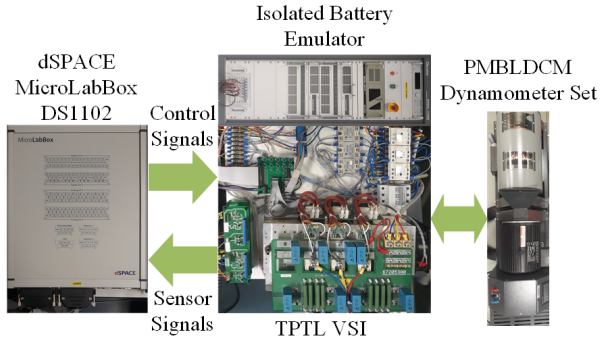

Fig. 12. Experimental hardware prototype of TPTL NPC VSI-driven PMBLDCM.

results of the transient speed and torque response are given in Fig. 9.

The active power requirement corresponds to the motor torque profile, and the zero reactive power ensures minimized power losses. The expanded view of simulation result for stator current both in the abc plane and $\alpha\beta$ plane is presented in Fig. 10 while applying sensorless MPC under steady state at load of 5 Nm. It is observed that the $\alpha\beta$ plane stator current generates petal-wave lissajous pattern at $\hat{\omega}_m = 500$ r/min and $\hat{\omega}_m = 1500$ r/min, as shown in Fig. 11(a) and (b). The simulation results of optimized stator phase back EMF for $\hat{\omega}_m = 500$ rpm and $\hat{\omega}_m = 1500$ r/min are shown in Fig. 11(a) and (b). These trajectories validate the theoretical analysis given in Section III proving reduced ripple.

B. Experimental Verification and Results

Fig. 12 shows an experimental hardware prototype. The overall drive system comprises of a TPTL NPC VSI,

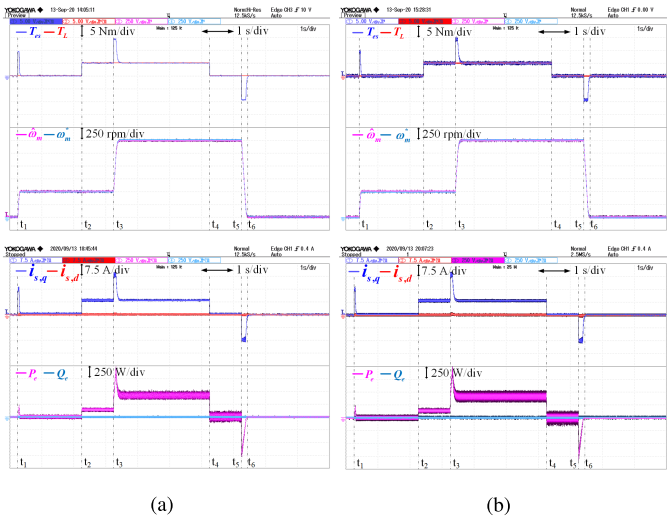

Fig. 13. Hardware results: T_{es}, T_L, $\hat{\omega}_m$, $\omega_m{}^*$, $i_{s,dq}$, P_e, and Q_e of (a) proposed MPC with iron loss and (b) vector control ignoring iron loss [20].

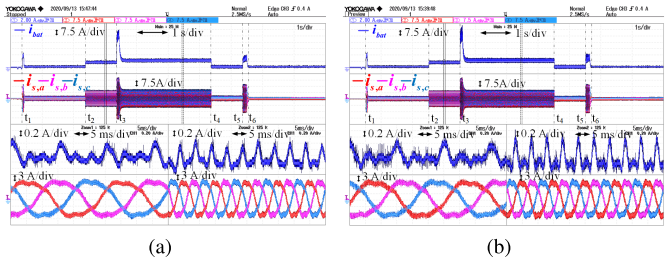

Fig. 14. Hardware results: i_{bat} and $i_{s,abc} = [i_{s,a},\ i_{s,b},\ i_{s,c}]'$ for (a) proposed MPC with iron loss and (b) vector control ignoring iron loss [20].

a PMBLDCM, and a digital control unit. The PMBLDCM is coupled to a dc machine that functions as load. The SKM100GB063D IGBT and SKKD100 fast recovery diode-based TPTL NPC VSI with 20-kHz switching frequency is used. A dc-link voltage of 240 V and 1000-Ah battery pack is used for powering VSI. Two current sensors (LEM LA55p) and two voltage sensor (LEM LV25p) are utilized to measure two-phase stator current and voltage across dc-link capacitors, respectively. The measured voltage and current signals are given to the digital controller dSPACE1102 in which the control algorithms are executed. The motor torque, motor speed, and active and reactive powers are estimated in real time using this digital controller. These signals are converted into analog signals using inbuilt digital-to-analog (DAC) converter and analyzed using digital storage oscilloscope. To demonstrate the effectiveness of the proposed modeling, the drive is evaluated experimentally for both the proposed sensorless MPC considering the iron loss and vector control with hall position sensors, ignoring iron loss as per [20]. The corresponding experimental results are given in Fig. 13. In both cases, identical conditions are maintained. The experimental results of T_{es}, $\hat{\omega}_m$, $i_{s,dq}$, P_e, and Q_e, under different operating conditions of both cases are given in Fig. 13. The PMBLDCM is accelerated from stand still to 500 rpm at t_1 with a step speed command under no load. The motor speed reaches its steady

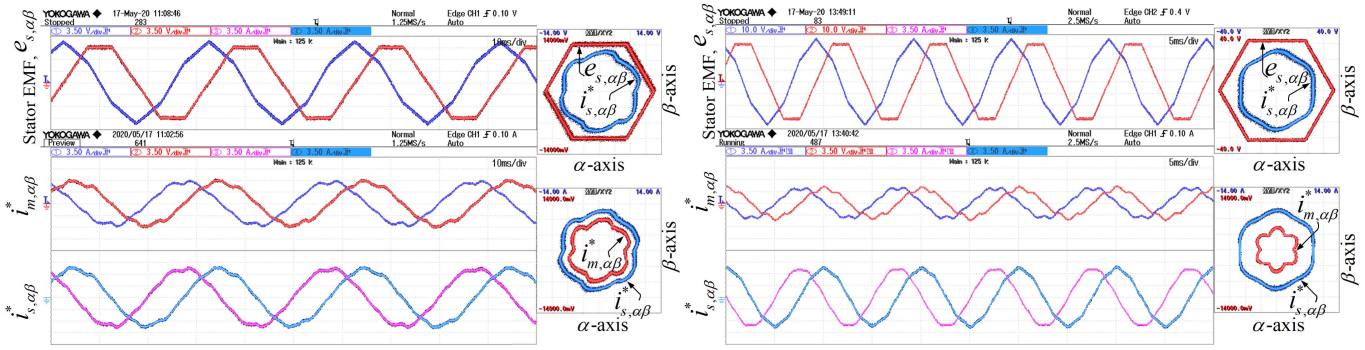

Fig. 15. Experimental results. Plot of $e_{s,\alpha\beta}$, $i^*_{s,\alpha\beta}$, and $i^*_{m,\alpha\beta}$ for the proposed MPC considering iron loss and vector control with lossless model [20] while running around (a) 500 and (b) 1500 r/min at 5 Nm.

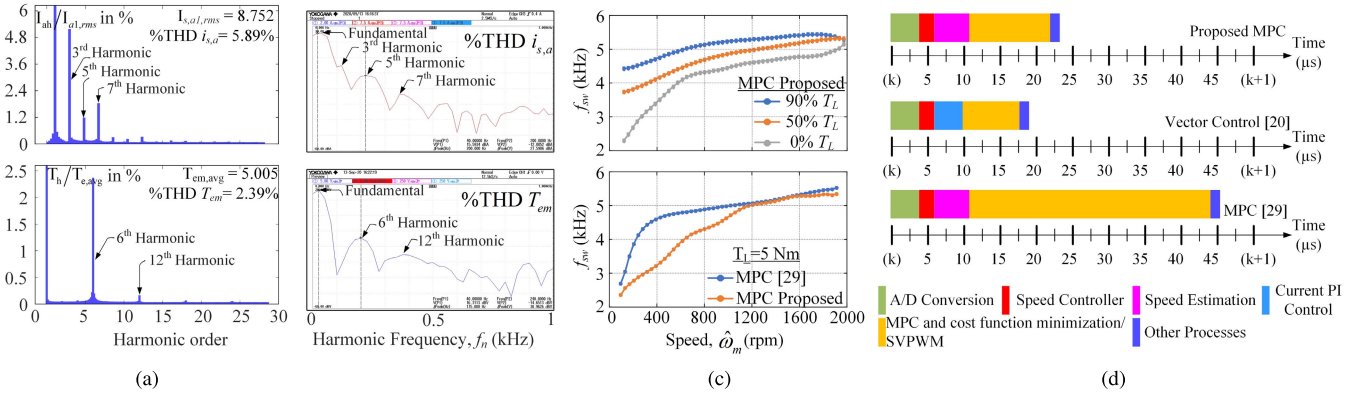

Fig. 16. Significant current and torque harmonics. (a) Simulation results. (b) Hardware results. (c) Switching frequency at various load torque. (d) Timing diagram of real-time implementation.

state in 70 ms in case of the proposed MPC controller and proves faster than the conventional vector control approach. At t_2, the load torque of $T_L = 5$ Nm is applied and $\hat{\omega}_m$ remains constant without any fluctuation and proves the faster dynamic of disturbance observer. At t_3, a step speed command of 500 to 1500 r/min is given with the load torque of 5 Nm and the steady-state speed of 1500 rpm after 170 ms. It can be observed that sudden load removal at t_4 does not affect motor speed output. At t_5, the proposed controller performs a regenerative action by detecting a sudden brake operation, and finally, the PMBLDCM achieves zero speed at t_6. The active power demand (P_e) follows T_{es}. The reactive power Q_e remains constant at zero, verifying that the phase current and phase back EMF are in phase. The plots of the stator current and the current drawn from the battery pack (i_{bat}) are shown in Fig. 14, which shows less ripple for the proposed algorithm. The time scale expanded results of these plots at steady state for $\hat{\omega}_m = 500$ r/min and $\hat{\omega}_m = 1500$ r/min with load torque of 5 Nm is presented for the proposed model with loss and the model without iron loss [20] in Fig. 14(a) and (b), respectively.

The plots of $e_{s,\alpha\beta}$ and $i_{s,\alpha\beta}$ with the proposed model with iron loss and without iron loss at $T_L = 5$ Nm are given in Fig. 15(a) and (b) for 500 and 1500 r/min, respectively. It can be found that the phase current waveforms appear like petal wave current with low ripple from the proposed method, which is in line with the theoretical observations. For the conventional method [20], where iron losses are neglected, the current trajectory shows high ripple. Current THD and torque THD are validated by both simulations and experiments, as shown in Fig. 16(a) and (b), respectively, during steady-state operation of the PMBLDCM with $T_L = 5$ Nm. The harmonic analysis shows the motor torque THD of 2.39% and the dominant harmonics are 6th and 12th harmonics with the magnitude of 2.3% and 0.1%, respectively. The ripple values computed from these experimental results for various variables are tabulated in Table III. The last column in Table III shows the % improvement in the ripple in T_{es}, P_e, Q_e, i_s^{abc}, and i_{bat}. These comparative results demonstrate the significant reduction in ripple of various parameters by the proposed method with iron loss when compared with that of [20] where iron losses are neglected, thus validating the

TABLE III

PERFORMANCE PARAMETER COMPARISON OF THE PROPOSED IRON-LOSS MODEL WITH LOSSLESS MODEL [20] AT 500 AND 1500 r/min

Change in Parameters (in %)	Proposed Iron-loss Model with proposed MPC controller		Lossless Model [20] with proposed MPC controller		% Improvement in proposed Iron-loss Model	
	500rpm	1500rpm	500rpm	1500rpm	500rpm	1500rpm
ΔT_{es}	3.1	3.5	6.9	7.6	55. 07	53.9
$\Delta\hat{\omega}_m$	3.1	7.4	4.6	12.6	32.6	41.2
ΔP	1.4	2.8	3.1	9.4	54.8	70.2
$\Delta I_{s,abc}$	3.6	6.9	7.8	10.8	53.8	36.1
ΔI_{bat}	9.2	12.1	11.1	14.1	17.1	14.1

analytical observations. The average switching frequency of an inverter is measured as count of switching pulses over 1-s time period. The average switching frequencies of the TPTL VSI when operated under the proposed MPC scheme are plotted with respect to speed variation in Fig. 16(c) (top), where the switching frequency versus rotor speed curves are plotted for different load torques. It is clear from Fig. 16(c) (top) that the average switching frequency increases with the increase of speed irrespective of load torque. The variation of average switching frequency with the variation of speed is plotted for the vector control scheme of [20] and the proposed MPC scheme both for a load torque of 5 Nm in Fig. 16(c) (bottom). It is observed from Fig. 16(c) (bottom) that the TPTL VSI is operated with lower average switching frequency when operated under the proposed MPC scheme compared with the vector control scheme mentioned in [20].

Fig. 16(d) shows the timing information of the proposed MPC technique in real-time implementation and compared with that of the MPC method [29] and vector control method [20]. The microprocessor specifications (timing, PWM generation, and so on) are imposed by the proposed MPC, MPC in [29], and vector control method [20]. However, the proposed MPC requires 11 μs from a computational point of view, MPC in [29] needs approximately 33 μs, and vector control [20] consumes just approximately 8 μs of the sampling time. The proposed MPC represents a clear advantage against MPC approach in [29], especially in low-powered drives, where switching frequencies (up to 20 kHz) are utilized. However, EV propulsion drives appear to be relatively medium powered, and thus, the sampling time of 50 μs does not create difficulties in practical operation.

V. Conclusion

An appropriate loss modeling of PMBLDCM with detailed analysis has been developed to achieve the control stability of EV for wide speed range at different road surface conditions. A sensorless scheme using a disturbance observer is carried out for high-precision drive control taking iron-loss component into account. A modified predictive control algorithm is validated for torque ripple-free operation of EV at reduced losses. In addition, the impact of iron loss on the optimal current vector has been investigated and the modified optimal current reference vector ensures low torque ripple and reduced losses. The efficient drive behavior employing the proposed model is demonstrated, validated with simulation and experimental findings. Consequently, the comparative experimental results that examine the effectiveness of the proposed method to that of the conventional method without considering iron loss are presented. The potential outcomes with the proposed algorithms, while considering the effect of iron losses, include the following.

1) Modified optimal current reference vector reduces torque ripple and the losses.
2) Reduced voltage stress on switches, reduced torque and current ripple, elimination of CMV, and improved THD using TPTL NPC VSI.
3) Significantly improved dynamics of EV with minimal steady-state error using disturbance observer to estimate motor speed.

This method yielded a high-performance solution with less computation burden, reduced torque ripple, and lower impact of losses on PMBLDCM. The results demonstrate the adequacy of the method for a 2.5-kW PMBLDCM proposed for EV applications.

References

[1] U. R. Muduli, A. R. Beig, K. A. Jaafari, J. Y. Alsawalhi, and R. K. Behera, "Interrupt free operation of dual motor four-wheel drive electric vehicle under inverter failure," *IEEE Trans. Transport. Electrific.*, early access, May 28, 2020, doi: 10.1109/TTE.2020.2997354.

[2] J. Pan, Y. Yang, J. Li, F. Wang, Y. Abdullah, and L. Xu, "Control of high-performance drive feeding by four-level hybrid clamped converter for transportation electrification," *IEEE Trans. Transport. Electrific.*, vol. 6, no. 2, pp. 568–577, Jun. 2020.

[3] A. Emadi, Y. Joo Lee, and K. Rajashekara, "Power electronics and motor drives in electric, hybrid electric, and plug-in hybrid electric vehicles," *IEEE Trans. Ind. Electron.*, vol. 55, no. 6, pp. 2237–2245, Jun. 2008.

[4] K. T. Chau, C. C. Chan, and C. Liu, "Overview of permanent-magnet brushless drives for electric and hybrid electric vehicles," *IEEE Trans. Ind. Electron.*, vol. 55, no. 6, pp. 2246–2257, Jun. 2008.

[5] S. Xue, J. Feng, S. Guo, J. Peng, W. Q. Chu, and Z. Q. Zhu, "A new iron loss model for temperature dependencies of hysteresis and eddy current losses in electrical machines," *IEEE Trans. Magn.*, vol. 54, no. 1, pp. 1–10, Jan. 2018.

[6] G. Liu, X. Chen, X. Zhou, and S. Zheng, "Sensorless commutation deviation correction of brushless DC motor with three-phase asymmetric back-EMF," *IEEE Trans. Ind. Electron.*, vol. 67, no. 7, pp. 6158–6167, Jul. 2020.

[7] C. Xia, B. Ji, and Y. Yan, "Smooth speed control for low-speed high-torque permanent-magnet synchronous motor using Proportional–Integral–Resonant controller," *IEEE Trans. Ind. Electron.*, vol. 62, no. 4, pp. 2123–2134, Apr. 2015.

[8] A. Ruf, S. Steentjes, A. Thul, and K. Hameyer, "Stator current vector determination under consideration of local iron loss distribution for partial load operation of PMSM," *IEEE Trans. Ind. Appl.*, vol. 52, no. 4, pp. 3005–3012, Jul. 2016.

[9] A. Frias, A. Kedous-Lebouc, C. Chillet, L. Albert, L. Calegari, and O. Messal, "Loss minimization of an electrical vehicle machine considering its control and iron losses," *IEEE Trans. Magn.*, vol. 52, no. 5, pp. 1–4, May 2016.

[10] J. Chen, D. Wang, S. Cheng, Y. Wang, Y. Zhu, and Q. Liu, "Modeling of temperature effects on magnetic property of nonoriented silicon steel lamination," *IEEE Trans. Magn.*, vol. 51, no. 11, pp. 1–4, Nov. 2015.

[11] S. Xue, W. Q. Chu, Z. Q. Zhu, J. Peng, S. Guo, and J. Feng, "Iron loss calculation considering temperature influence in non-oriented steel laminations," *IET Sci., Meas. Technol.*, vol. 10, no. 8, pp. 846–854, Nov. 2016.

[12] M. Fasil, N. Mijatovic, B. B. Jensen, and J. Holboll, "Nonlinear dynamic model of PMBLDC motor considering core losses," *IEEE Trans. Ind. Electron.*, vol. 64, no. 12, pp. 9282–9290, Dec. 2017.

[13] Y. Wang, X. Zhang, X. Yuan, and G. Liu, "Position-sensorless hybrid sliding-mode control of electric vehicles with brushless DC motor," *IEEE Trans. Veh. Technol.*, vol. 60, no. 2, pp. 421–432, Feb. 2011.

[14] A. Dadashnialehi, A. Bab-Hadiashar, Z. Cao, and A. Kapoor, "Intelligent sensorless antilock braking system for brushless in-wheel electric vehicles," *IEEE Trans. Ind. Electron.*, vol. 62, no. 3, pp. 1629–1638, Mar. 2015.

[15] T. Li and J. Zhou, "High-stability position-sensorless control method for brushless DC motors at low speed," *IEEE Trans. Power Electron.*, vol. 34, no. 5, pp. 4895–4903, May 2019.

[16] M. Jafarboland and M. H. R. Silabi, "New sensorless commutation method for BLDC motors based on the line-to-line flux linkage theory," *IET Electric Power Appl.*, vol. 13, no. 6, pp. 703–711, Jun. 2019.

[17] X. Song, B. Han, S. Zheng, and J. Fang, "High-precision sensorless drive for high-speed BLDC motors based on the virtual third harmonic back-EMF," *IEEE Trans. Power Electron.*, vol. 33, no. 2, pp. 1528–1540, Feb. 2018.

[18] A. Apte, V. A. Joshi, H. Mehta, and R. Walambe, "Disturbance-Observer-Based sensorless control of PMSM using integral state feedback controller," *IEEE Trans. Power Electron.*, vol. 35, no. 6, pp. 6082–6090, Jun. 2020.
[19] A. Damiano, A. Floris, G. Fois, I. Marongiu, M. Porru, and A. Serpi, "Design of a high-speed ferrite-based brushless DC machine for electric vehicles," *IEEE Trans. Ind. Appl.*, vol. 53, no. 5, pp. 4279–4287, Sep. 2017.
[20] G. Buja, M. Bertoluzzo, and R. K. Keshri, "Torque ripple-free operation of PM BLDC drives with petal-wave current supply," *IEEE Trans. Ind. Electron.*, vol. 62, no. 7, pp. 4034–4043, Jul. 2015.
[21] P. Kumar, D. V. Bhaskar, R. K. Behera, and U. R. Muduli, "A modified torque ripple minimization technique for BLDC motor drive using synthesized current phase compensation," in *Proc. IEEE Int. Conf. Ind. Technol. (ICIT)*, Feb. 2020, pp. 127–132.
[22] S. B. Ozturk and H. A. Toliyat, "Direct torque and indirect flux control of brushless DC motor," *IEEE/ASME Trans. Mechatronics*, vol. 16, no. 2, pp. 351–360, Apr. 2011.
[23] M. Lee and K. Kong, "Fourier-series-based phase delay compensation of brushless DC motor systems," *IEEE Trans. Power Electron.*, vol. 33, no. 1, pp. 525–534, Jan. 2018.
[24] A. A. Ahmed, B. K. Koh, and Y. I. Lee, "A comparison of finite control set and continuous control set model predictive control schemes for speed control of induction motors," *IEEE Trans. Ind. Informat.*, vol. 14, no. 4, pp. 1334–1346, Apr. 2018.
[25] H. T. Nguyen and J.-W. Jung, "Finite control set model predictive control to guarantee stability and robustness for surface-mounted PM synchronous motors," *IEEE Trans. Ind. Electron.*, vol. 65, no. 11, pp. 8510–8519, Nov. 2018.
[26] A. G. de Castro, W. C. A. Pereira, T. E. P. de Almeida, C. M. R. de Oliveira, J. R. B. de Almeida Monteiro, and A. A. de Oliveira, "Improved finite control-set model-based direct power control of BLDC motor with reduced torque ripple," *IEEE Trans. Ind. Appl.*, vol. 54, no. 5, pp. 4476–4484, Sep. 2018.
[27] A. G. Castro *et al.*, "Finite control-set predictive power control of BLDC drive for torque ripple reduction," *IEEE Latin Amer. Trans.*, vol. 16, no. 4, pp. 1128–1135, Apr. 2018.
[28] X. Wang *et al.*, "Deadbeat predictive current control based fault-tolerant scheme for dual three-phase PMSM drives," *IEEE J. Emerg. Sel. Topics Power Electron.*, early access, Mar. 27, 2020, doi: 10.1109/JESTPE.2020.2983691.
[29] R. E. K. Meesala, V. P. K. Kunisetti, and V. K. Thippiripati, "Enhanced predictive torque control for open end winding induction motor drive without weighting factor assignment," *IEEE Trans. Power Electron.*, vol. 34, no. 1, pp. 503–513, Jan. 2019.
[30] R. Sreejith and B. Singh, "Sensorless predictive current control of PMSM EV drive using DSOGI-FLL based sliding mode observer," *IEEE Trans. Ind. Electron.*, early access, May 27, 2020, doi: 10.1109/TIE.2020.2996159.
[31] V. Viswanathan and J. Seenithangom, "Commutation torque ripple reduction in the BLDC motor using modified SEPIC and three-level NPC inverter," *IEEE Trans. Power Electron.*, vol. 33, no. 1, pp. 535–546, Jan. 2018.
[32] N. Urasaki, T. Senjyu, and K. Uezato, "Investigation of influences of various losses on electromagnetic torque for surface-mounted permanent magnet synchronous motors," *IEEE Trans. Power Electron.*, vol. 18, no. 1, pp. 131–139, Jan. 2003.

Prashant Kumar (Graduate Student Member, IEEE) received the B.Tech. degree in electrical and electronics engineering from the Guru Ramdas Khalsa Institute of Science and Technology, Jabalpur, India, in 2012, and the M.Tech. degree in electrical engineering from IIT (Indian School of Mines) Dhanbad, Dhanbad, India, in 2018. He is currently working on his Ph.D. thesis at IIT (Indian School of Mines) Dhanbad.

He was a Visiting Scholar with the Department of Electrical Engineering and Computer Science, Khalifa University, Abu Dhabi, United Arab Emirates, in 2020. His research interests include modulation strategies for permanent-magnet brushless dc (PMBLDC) motor drives and its control, and sensorless predictive control.

Devara Vijaya Bhaskar (Member, IEEE) received the B.Tech. degree in electrical and electronics engineering from Jawaharlal Nehru Technological University, Hyderabad, India, in 2006, and the M.Tech. degree in power electronics and drives and the Ph.D. degree in electrical engineering from the National Institute of Technology, Warangal, India, in 2009 and 2017, respectively.

He is currently working as an Assistant Professor with the Department of Electrical Engineering, IIT (Indian School of Mines) Dhanbad, Dhanbad, India. His research interests include low-cost drive converters for electric vehicle and household appliances, and nonlinear control.

Utkal Ranjan Muduli (Member, IEEE) received the B.Tech. degree in electrical and electronics engineering from the Biju Patnaik University of Technology Odisha, Rourkela, India, in 2011, and the M.Tech. degree in electrical engineering from IIT Gandhinagar, Palaj, India, in 2014. He is currently working on his Ph.D. thesis at IIT Patna, Patna, India.

He was a Visiting Scholar with the Department of Electrical Engineering and Computer Science, Khalifa University, Abu Dhabi, United Arab Emirates, in 2019. His research interests include modulation strategies for multiphase motor drives, matrix converters and its control, battery power management, and wireless power transfer.

Abdul R. Beig (Senior Member, IEEE) received the B.Eng. degree in electrical and electronics engineering from the National Institute of Technology Karnataka, Surathkal, India, in 1989, and the M.Tech. and Ph.D. degrees in electrical engineering from the Indian Institute of Science, Bengaluru, India, in 1998 and 2004, respectively.

He is currently an Associate Professor with the Advanced Power and Energy Center, Electrical Engineering and Computer Science Department, Khalifa University of Science and Technology, Abu Dhabi, United Arab Emirates. His current research focus is on autotuning of grid-connected converters, electric vehicles dive trains, high-gain converters, modular multilevel converters, and SiC-based converters.

Dr. Beig has been serving as an Associate Editor for the IEEE TRANSACTIONS ON INDUSTRY APPLICATIONS.

Ranjan Kumar Behera (Senior Member, IEEE) received the B.Eng. degree in electrical engineering from the Regional Engineering College (NIT) Rourkela, Rourkela, India, in 1998, and the M.Tech. and Ph.D. degrees from IIT Kanpur, Kanpur, India, in 2003 and 2009, respectively.

He was a Visiting Scholar with the Energy Systems Research Center, Tennessee Technological University, Cookeville, TN, USA, in 2008. Since 2009, he has been a Faculty Member with the Department of Electrical Engineering, IIT Patna, Patna, India, where he is currently an Associate Professor. In July 2016, he was a Visiting Research Collaborator with the Department of Electrical, Electronic and Computer Engineering, University of Pretoria, Pretoria, South Africa. He is the author of more than 100 scientific papers published in conference proceedings and international journals. His research interests include nonlinear control theory application to power electronic converters, pulsewidth modulation techniques, and multiphase electric drives control.

Dr. Behera has received many national and international awards, such as the Young Scientists Award in engineering sciences, DST, Government of India, in 2001, the Bhaskara Advanced Solar Energy (BASE) Indo-U.S. Science and Technology Forum for Solar research in USA, in 2014, and selected as the Featured Engineer of the Globe in 2015.